PCCP

Accepted Manuscript

ROYAL SOCIETY OF CHEMISTRY

www.rsc.org/pccp

Journal Name

ARTICLE TYPE

Cite this: DOI: 10.1039/xxxxxxxxxx

Catalytic potential of highly defective (211) surfaces of zinc blende ZnO

Chunguang Tang,*[a] Hugh F. Wilson,[b,c] Michelle J. S. Spencer,[b,c] and Amanda S. Barnard[b]

Received Date
Accepted Date

DOI: 10.1039/xxxxxxxxxx

www.rsc.org/journalname

Zinc blende (ZB) ZnO has gained increasing research interests due to its favorable properties and its stabilization in nanoscale. While surface properties are important in nanoscale, the studies on ZB ZnO surface properties are sparse. Here we have performed first principles calculations of the energies and structures of ZB and wurtzite (WZ) ZnO surfaces. Our results indicate that, among the four surfaces parallel to the polar axes, such as $(10\bar{1}0)$ and $(11\bar{2}0)$ of WZ phase and (110) and (211) of ZB phase, the polar (211) surface has substantially lower surface vacancy formation energies than the others, which makes ZB ZnO promising for catalytic applications. Our results also imply the stabilization of ZB ZnO in nanoscale is due to some mechanisms other than surface energies.

1 Introduction

Zinc oxide (ZnO) has been the subject of extensive research interest due to its electrical, optical, and catalytic properties. The applications of ZnO at the nanoscale critically depend on its surface properties, and hence many experimental[1–3] and theoretical[4–8] studies on the surface properties have been carried out. These studies have mainly focused on the surfaces of the hexagonal wurtzite (WZ) phase, and significantly less attention has been devoted to those of the cubic zinc blende (ZB) ZnO. This is due to the fact that under ambient conditions, bulk ZnO is in its WZ phase, and the ZB phase is metastable. Nevertheless, it is desirable to synthesize ZB ZnO due to its favorable properties for electronic and optoelectronic applications.[9–13] It exhibits lower carrier scattering, due to its high crystallographic symmetry, and higher p-type doping efficiencies than WZ ZnO.[11] It also shows brighter band-edge luminescence at room temperature.[9,10] ZnO in the ZB phase is usually synthesized in film form using substrates such as ZnS/GaAs[11], and $Pt/Ti/SiO_2/Si$[10]. Other forms of ZB ZnO have also been observed in nanoscale.[12,14–16] For example, pure ZB ZnO nanorods were synthesized using silicon substrate[12] and the ZB phase was found in the legs of tetrapod nanoparticles.[15]

A good understanding of the surface properties of ZB ZnO is necessary for engineering of nanoscale particles and devices based on ZB ZnO. Experimentally it is challenging to study the properties of a specific surface, and so the measured properties such as surface energies are averaged over all exposed ZnO surfaces.[17,18] This makes theoretical calculation a favorable option. Based on first principles computations we previously estimated the energies of the Zn- and O-terminated ZB (111) surfaces, separately, and found them similar to their WZ (0001) counterparts.[19] As these polar surfaces have energies much higher than those of nonpolar surfaces, ZnO particle surfaces are dominated by the facets that are parallel to the polar axes, such as $(10\bar{1}0)$ and $(11\bar{2}0)$ for WZ phase and (110) and (211) for ZB phase. While the other three nonpolar surfaces are well studied, (211) is sparsely investigated although it is, like (110), believed to be a possible exposed surface of ZB ZnO nanowires.[14] As surfaces are important for stabilizing high energy phases at the nanoscale, studies of (110) and (211) would help our understanding of the existence of the ZB phase in the tetrapod ZnO nanoparticles.[15]

Recently the energies of ZB ZnO surfaces were computed and compared with those of WZ phase and rocksalt phase.[20] The authors found the energy of the ZB (110) face is about 50% higher than that of WZ $(11\bar{2}0)$. This is surprising as these two surfaces have similar structures. When viewed down the polar axes, the

[a] School of Materials Science and Engineering, University of New South Wales, NSW 2052, Australia. E-mail: chunguang.tang@unsw.edu.au or 0123.tang@gmail.com
[b] Virtual Nanoscience Laboratory, CSIRO, Parkville, VIC 3052, Australia.
[c] School of Applied Sciences, RMIT University, Melbourne VIC 3001, Australia

cutting of a Zn-O bouble-layer along faces $(11\bar{2}0)$ and (110) results in armchair boundaries, and the cutting along faces $(10\bar{1}0)$ and (211) results in zigzag boundaries, as shown in Fig. 1. Hence, it would be appealing to expect that faces (110) and (211) have surface properties similar to those of $(11\bar{2}0)$ and $(10\bar{1}0)$, respectively.

In this work we study ZB ZnO surfaces (110) and (211) together with their counterparts in the WZ phase with first principles computations based on density functional theory, as used in ref.[20]. Our calculations reveal that (110) and $(11\bar{2}0)$ have nearly identical surface energies, slightly higher than that of $(10\bar{1}0)$. Different from the other three surfaces, (211) has a noticeably higher surface energy due to its polarity and has very low formation energies of Zn and O vacancies, which makes it promising for catalytic applications. Our results also imply the nanoscale ZB ZnO is stabilized by some mechanism other than surface energies.

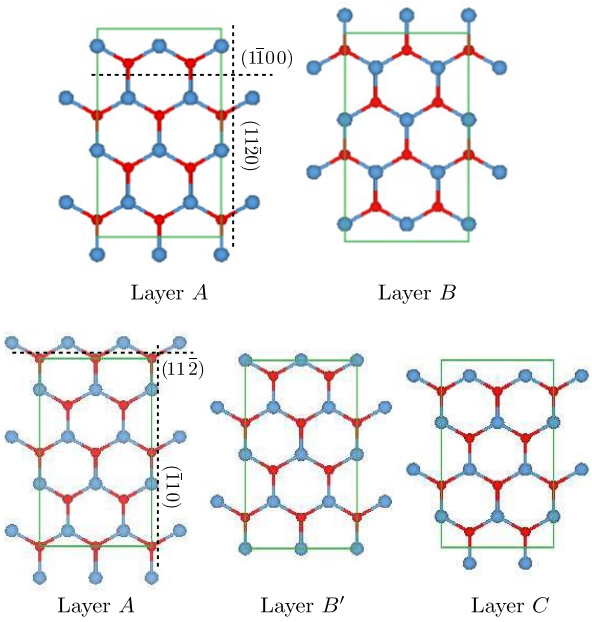

Fig. 1 (top) WZ Zn-O double-layer stacking $\cdots ABAB\cdots$ along [0001]. (bottom) ZB Zn-O double-layer stacking $\cdots AB'CAB'C\cdots$ along [111]. The dashed lines indicate the surfaces that are perpendicular to the paper. Note that, due to symmetry, $(1\bar{1}00)$ is equivalent to $(10\bar{1}0)$, and $(11\bar{2})$ and $(\bar{1}10)$ are equivalent to (211) and (110), respectively. Red: O, blue: Zn.

2 Methods

Often surface energies are calculated by comparing the energies of an atomic slab and the ideal bulk structure. Based on this approach the surface energy γ can be defined as

$$\gamma = \frac{E_s - n_{Zn}\mu_{Zn} - n_O\mu_O}{2A} \quad (1)$$

Table 1 Calculated and experimental lattice parameters for WZ and ZB ZnO. For ideal WZ crystal, $c/a = \sqrt{8/3}$ and $u = 3/8$.

Phase	Source	a (Å)	c (Å)	c/a	u
WZ	This work	3.2862	5.3005	1.6130	0.3793
	Expt. (Ref.[22])	3.2496	5.2042	1.6018	0.3819
	Expt. (Ref.[23])	3.2501	5.2071	1.6021	0.3817
ZB	This work	4.6272			
	Expt. (Ref.[24])	4.37∼4.47			

where E_s is the calculated total energy of the ZnO slab, n is the number of atoms in the slab, and $2A$ is the area of the two surfaces of the slab. The chemical potentials μ_{Zn} and μ_O in ZnO can vary in a range constrained by the facts that Zn and O are in equilibrium with bulk ZnO and that bulk ZnO is stable against decomposition into bulk Zn and oxygen gas. Explicitly, one has $\mu_{Zn} + \mu_O = E_{ZnO}$, $\Delta H_{ZnO} \le \Delta\mu_O = \mu_O - 0.5E_{O_2} \le 0$ and $\Delta H_{ZnO} \le \Delta\mu_{Zn} = \mu_{Zn} - E_{Zn}^{bulk} \le 0$, where E is the calculated total energy at 0 K, and the formation enthalpy $\Delta H_{ZnO} = E_{ZnO} - 0.5E_{O_2} - E_{Zn}^{bulk}$ is calculated to be -2.89 eV, compared with previously calculated value[5] of -2.84 eV and experimental value[21] -3.50 eV. The oxygen in ZnO is assumed to be in equilibrium with the ambient atmosphere, and hence $\mu_O = 0.5\mu_{O_2}$ is a function of temperature and pressure.

The above definition of surface energy implicitly requires the two surfaces to have identical structures. For polar slabs of which the two sides are different, this definition gives an averaged surface energy for two different surfaces. For calculating the surface energy of a single polar surface, we refer the readers to our recent work[19] and references therein.

For slabs with an equal number of Zn and O atoms, which is true for the four surfaces considered here, Eq. (1) can be simplified as

$$\gamma = \frac{E_s - n \times E_{ZnO}}{2A} \quad (2)$$

where n is the number of ZnO units included in the slab and E_{ZnO} is the energy of a ZnO unit in the corresponding ideal bulk structure.

For surface calculations, supercell slab models with periodic boundary conditions were used (Fig. 2). Along the surface plane, 2×2 and 2×1 supercells were used for WZ and ZB phases, respectively, to allow for somewhat reconstruction, and along the surface normal, the slab of various number of atom layers is separated from its periodic images by a vacuum layer more than 15 Å. In these slab models all atoms were allowed to move except for the central two layers of atoms, which were fixed along the surface normal.

For surface defects, we considered oxygen and zinc vacancies. The formation energy, E_f, of an isolated surface vacancy can be defined as

$$E_f = E_{sv} + \mu_x - E_s \quad (3)$$

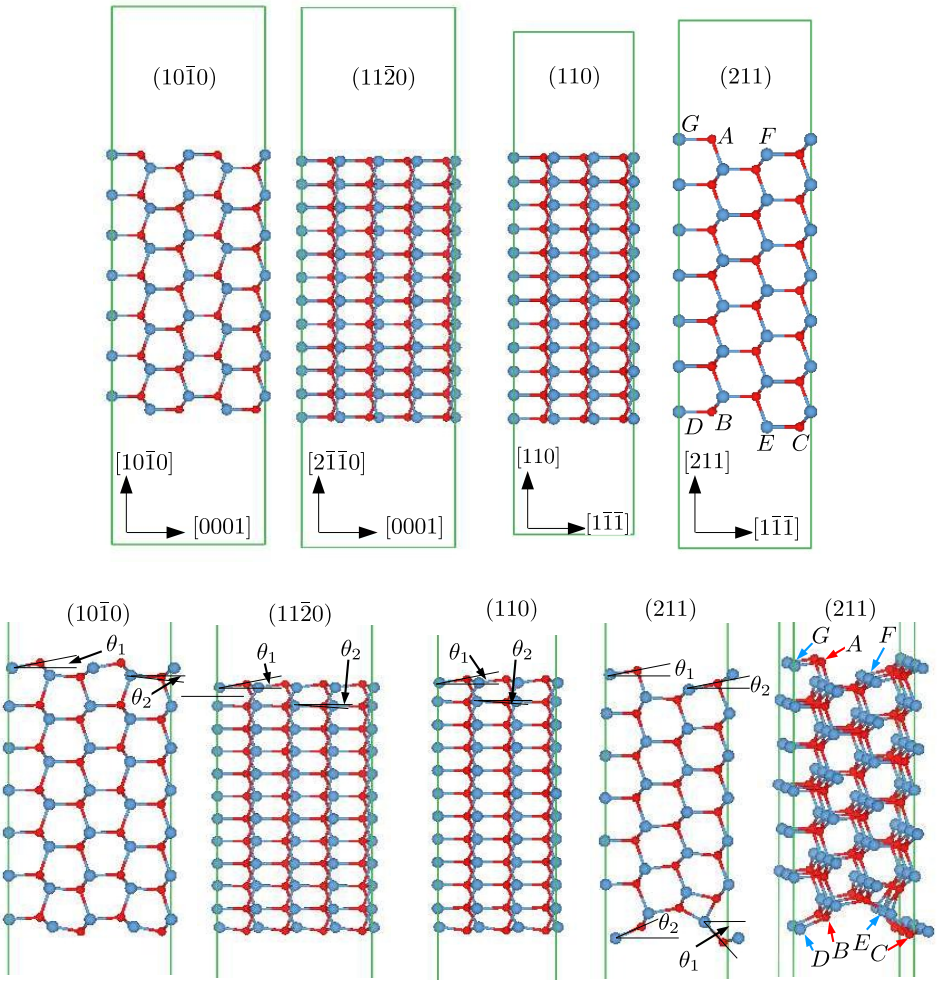

Fig. 2 Surface model structures before (top) and after (bottom) geometry optimization. From left to right in the top panel, the number of atomic layers in the slabs are 14, 12, 12, and 20. θ is defined as the angle between the Zn-O bond in the same atom layer and the surface plane, and has a positive value when the O atom is farther from the slab center. θ_1 and θ_2 are for outermost and second outermost layers, respectively. Red: O, blue: Zn.

where E_{sv} and E_s are the energies of the slab with and without a surface vacancy, respectively, and subscript x represents vacancy species (O or Zn). Larger supercells were used so that an isolated vacancy is separated from its periodic images in the surface plane by at least 10.6 Å.

The total energy calculations are performed using the VASP code[25] with projector-augmented-wave pseudopotentials[26,27] as supplied in VASP, the generalized gradient approximation exchange-correlation functional of Perdew, Burke, and Ernzerhof (GGA-PBE)[28] and a plane wave basis set with an energy cutoff of 500 eV. For Brillioun zone integrations k-point sampling meshes of $6\times6\times4$ and $5\times5\times5$ were used for the hexagonal unit cell of WZ phase and the cubic unit cell of ZB phase, respectively, and the number of k-points was reduced for larger cells. For surface calculations only one k-point was used in the surface normal direction which involves vacuum. Through out all geometry optimizations the forces on atoms were converged to below 5 meV/Å. As shown in Table 1, the bulk structure parameters optimized under these settings are in good agreement with their experimental values.

3 Results and discussion

We calculated the surface energy γ of the four surfaces as a function of the slab thickness, and found that convergence of surface energies of (10$\bar{1}$0), (11$\bar{2}$0), and (110) is reached within 0.2 J/m^2 for slabs with more than 10 atomic layers, and for (211) the energy converges well for more than 16 atomic layers. By plotting the energies with respect to the reciprocal slab thickness[4] we have obtained the extrapolated surface energies for infinitely thick slabs to be 0.84, 0.87, 0.87 and 1.37 J/m^2 for (10$\bar{1}$0), (11$\bar{2}$0), (110), and (211), respectively. The values of (10$\bar{1}$0) and

Table 2 Surface energies γ, dangling bond density ρ, and tilt angle θ of ZnO surfaces calculated in this work and comparison with other theoretical studies. γ is extrapolated to infinitely thick slabs. For analytical values of ρ, d is the Zn-O bond length of ideal crystal structures. Relaxed crystal structures were used to calculate numerical ρ values. θ_1 and θ_2 are for outermost and second outermost layers, respectively. For the (211) surface the θ values in parentheses are for the bottom surface in Fig. 2.

	$(10\bar{1}0)$	$(11\bar{2}0)$	(110)	(211)	Comment
γ (J/m^2)	0.839	0.872	0.875	1.365	This work, GGA-PBE
	0.833	0.881			Ref.[8], GGA-PBE
	0.917	1.061			Ref.[4], GGA-PBE
	1.581	1.849			Ref.[4], LDA
	0.94	0.98	1.49		Ref.[20], GGA-PBE + U
	2.55±0.23 (averaged over all exposed surfaces)				Ref.[17,18], experiment for WZ phase
ρ	$\frac{3\sqrt{3}}{8\sqrt{2}}d^{-2}$	$\frac{3}{4\sqrt{2}}d^{-2}$	$\frac{3}{4\sqrt{2}}d^{-2}$	$\frac{\sqrt{3}}{\sqrt{8}}d^{-2}$	This work, for details see Appendix.
ρ (Å^{-2})	0.115	0.133	0.132	0.153	This work
θ_1 (°)	10.6	7.8	7.7	8.4 (48.0)	This work
	10.1	7.4			Ref.[4], GGA-PBE
	10.7	7.6			Ref.[4], LDA
	9.6	7.5			Ref.[29], GGA-PW91
θ_2 (°)	−3.7	−1.5	−1.5	12.5 (−24.7)	This work

$(11\bar{2}0)$ are supported by previous work, as shown in Table 2.

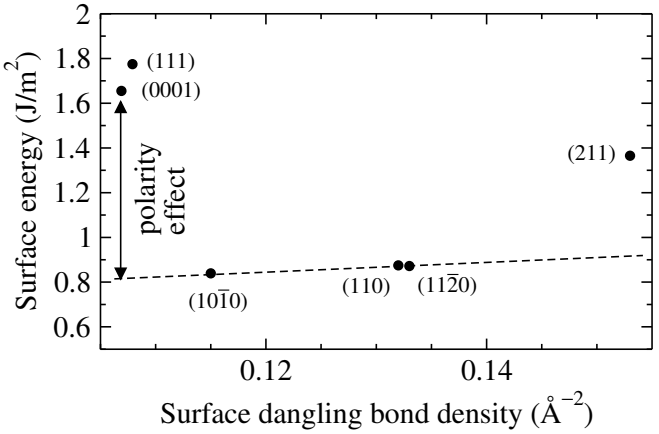

Fig. 3 Relationship between surface energy and surface dangling bond density for defect-free surfaces. Each surface is represented by a solid circle. The dashed line is a guide for the eye. For (111), (0001), and (211), the energy part above the dashed line can be considered as polarity contribution.

The surface energy of nonpolar surfaces results mainly from breaking the atomic bonds when creating the surfaces, or, in other words, γ depends on ρ, the density of surface dangling bonds, which is defined as the number of dangling bonds in a surface divided by the surface area. As shown in Table 2, $(11\bar{2}0)$ has ρ slightly higher than that of $(10\bar{1}0)$, and so it has slightly higher γ. Surfaces $(11\bar{2}0)$ and (110) have nearly identical ρ and γ, which is consistent with the fact that both of them have an armchair configuration. Surprisingly, surface (211) exhibits a substantially higher surface energy that is inconsistent with its dangling bond density. In Fig. 3 we have plotted γ and ρ for all the four surfaces, together with data for polar (0001) and (111) surfaces. For (0001) and (111), if we regard the energy portion indicated by the arrow as polarity contribution, the polarity contributes substantially (about 50%) to the energies of these two surfaces. Following this argument, it is obvious that (211) is a polar surface, with polarity contribution of about 30%.

To identify the origin of the polarity of (211), we refer to its surface structure. As shown in Fig. 2(top), in the top surface of the unrelaxed (211) slab, O atom at site *A* has two dangling bonds, and Zn atoms at sites *G* and *F* have one dangling bond each. Similarly, for the bottom surface, Zn atom at site *E* has two dangling bonds, and O atoms at sites *B* and *C* has one. Although each surface has in total an equal number of Zn- and O- dangling bonds, which probably is the reason that sometimes (211) is regarded as a nonpolar surface,[14] the presence of the surface ions in different planes results in a surface dipole. For the other three surfaces considered here, all surface Zn cations and O anions have one dangling bond and locate in the same plane (in the truncated unrelaxed structure) and thus no surface dipole is formed.

The high dangling bond density and the polarity of the (211) surface result in much more substantial surface relaxation and reconstruction compared with the other three surfaces. This is exemplified by the Zn-O bond tilt angle θ, which results from the different amount of relaxation of Zn and O along the surface normal, as shown in Fig. 2. For $(10\bar{1}0)$ and $(11\bar{2}0)$, Zn atoms in the outermost layer relax towards the bulk more than their O counterparts do, producing a tilt angle θ_1 about 10.6° and 7.8°, respectively, and in the second outermost layer, Zn atoms are farther than O atoms from the bulk, hence producing a negative tilt angle θ_2 about −3.7° and −1.5°, respectively. The tilt angles of

(110) are similar to those of $(11\bar{2}0)$, as shown in Table 2. For (211), θ_1 and θ_2 are about 8° and 13°, respectively, for the side where O anions have two dangling bonds (top side in Fig. 2). On the other side, the angles are far more larger, being 48° and −25°. The huge tilt angles result from the fact that the outermost Zn cations, which have two dangling bonds in the truncated surface, squeeze into the bulk and create a severely distorted local structure.

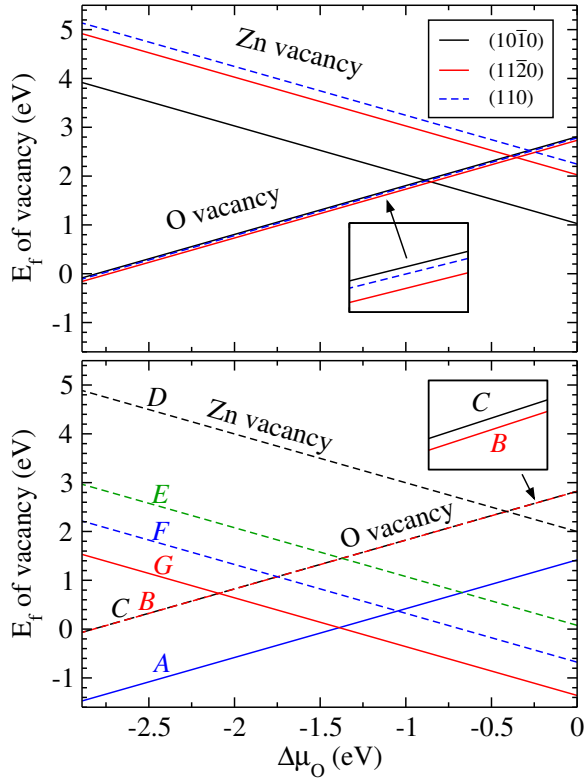

Fig. 4 Formation energy for an isolated vacancy on nonpolar surfaces (top) and polar surface (211) (bottom) as a function of oxygen chemical potential.ãĂĂFor (211), the formation energy depends on the location of the vacancy.

Fig. 4 shows the formation energies of an isolated surface vacancy on each surface. For the nonpolar surfaces, the formation energies of oxygen vacancies on the three surfaces are very close, and are only slightly negative at the oxygen poor limit. For the Zn vacancy, the formation energy on $(10\bar{1}0)$ is about 1 eV lower than those on $(11\bar{2}0)$ and (110) as one of the oxygen neighbors of the vacancy on $(10\bar{1}0)$ reduces its dangling bonds by approaching the Zn on the next Zn-O double-layer along the polar axis. The formation energies of O and Zn vacancies on $(10\bar{1}0)$ and $(11\bar{2}0)$ have been studied theoretically.[8,30] Our results are consistent with those reported by D'Amico *et al*[8], but the energy for the Zn vacancy on $(10\bar{1}0)$ is about 0.5 eV higher than that reported by Kováčik *et al*.[30]

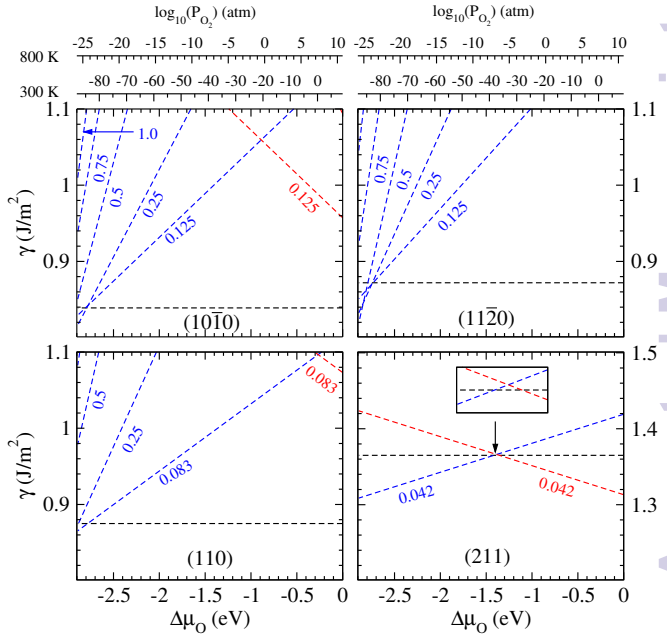

Fig. 5 Surface energies of $(10\bar{1}0)$, $(11\bar{2}0)$, (110), and (211) with various vacancy densities as a function of $\Delta\mu_O$. The surfaces defect-free, with O and Zn vacancies are in black, blue, and red, respectively. The numbers indicate surface defect densities. The total O (or Zn) sites on two sides of the slabs are 16, 16, 24, and 24 for defect-free $(10\bar{1}0)$, $(11\bar{2}0)$, (110), and (211), respectively. The pressure of O_2 corresponding to $\Delta\mu_O$ is shown for temperatures 300 K and 800 K, respectively.

Vacancy formation on surface (211) is different from those on the three nonpolar surfaces in two aspects. Firstly, the formation energy of a vacancy on the nonpolar surfaces is independent of its location, since all surface atoms of the same species are equivalent. For (211), however, the formation energies are sensitive to the vacancy location. Secondly, the formation energies of the O vacancy at site *A* and Zn vacancies at sites *E*, *F*, and *G* are much lower than their counterparts on the nonpolar surfaces. Fig. 4 (bottom) shows the formation of vacancies on surface (211) is thermodynamically favorable even at moderate processing conditions, i.e., not extremely O rich or poor.

To take into account the possible interactions among the defects, we have also calculated the energies of surfaces with several vacancy densities ranging from 0 to 1. For the nonpolar surfaces, we created vacancies on one side of the slab, with the other side fixed. We found the vacancy formation energy in this simplified case is similar to that with vacancies on both sides. In this case, the densities of O vacancy, for example, are defined as the ratio of vacancy sites to O sites on one side of the defect-free slab. For (211) where the two sides are different, the densities are defined as the ratio of vacancy sites to O sites on both sides. As shown in Fig. 5, for the nonpolar surfaces, the clean structures are stable

for a large range of μ_O, and oxygen deficient surfaces are preferred at the lower μ_O limit or the extremely reducing atmosphere, which is consistent with the isolated vacancy results above and with previous theoretical studies of $(10\bar{1}0)$ and $(11\bar{2}0)$.[8] On surface (211), a low density of O and Zn vacancies is prefered at oxygen poor and rich conditions, respectively.

Overall, the above results indicate that O vacancies on nonpolar surfaces are only thermodynamically favorable at the oxygen poor limit and Zn vacancies are unfavorable in the whole μ_O range. It should be pointed out that, although thermodynamically metastable, these surface defects can exist in thermodynamic equilibrium at temperatures above 0 K with defect concentrations dependent on their formation energies and temperature. Experimentally, the observation of both defective and defect-free nonpolar surfaces has been reported. Göpel *et al*[31,32] have produced O vacancies on $(10\bar{1}0)$ by heat treatment, surface photolysis, and surface reactions. Recently Fabbri *et al*[33] claimed that Zn vacancies on $(10\bar{1}0)$ induce green luminescence of ZnO nanostructures. In addition, vacancies of Zn-O dimers[34] have also been reported. On the other hand, scanning tunneling microscopy characterazations[34,35] of $(10\bar{1}0)$ and $(11\bar{2}0)$ have reported no signature of surface vacancies. Our results indicate that, compared with the nonpolar surfaces, (211) is more likely to possess surface vacancies. As surface vacancies are crucial to catalytic activity,[36–38] this makes (211) a promising surface for catalytic applications.

From Fig. 5 it is clear that the energies of ZB (211) are higher than those of WZ $(10\bar{1}0)$, for both clean and defective surfaces. While the energies of the clean (110) and $(11\bar{2}0)$ surfaces are similar, the $(11\bar{2}0)$ surface is more stable in the defective case. This implies that the stabilization of ZB ZnO in tetrapod nanoparticles[15] is due to some mechanism other than pure surface energies. One of the possibilities could be surface contamination by gas molecules, which deserves further investigation. Especially, recent experiments show that ZnO surfaces have a strong affinity to CO_2.[39]

4 Summary

We have performed first principles calculations of the energies and structures of four surfaces of ZnO: $(10\bar{1}0)$ and $(11\bar{2}0)$ for wurtzite phase and (110) and (211) for zinc blende phase. Among these four surfaces that are parallel to the polar axes, $(10\bar{1}0)$, $(11\bar{2}0)$, and (110) have similar surface energies, and (211) possesses higher energy due to its surface polarity. The formation energies of vacancies are positive for the nonpolar surfaces in the major range of oxygen chemical potential μ_O but can be negative for (211) in a wide μ_O range. We conclude that the overall higher surface energies of ZB ZnO do not contribute to its stabilization in nanoscale and the highly defective state of (211) makes it very promising for catalytic applications.

5 Acknowledgements

The authors acknowledge NCI National Facility for computational support of project code q27. The crystal structure drawings were produced using code VESTA.[40]

6 Appendix

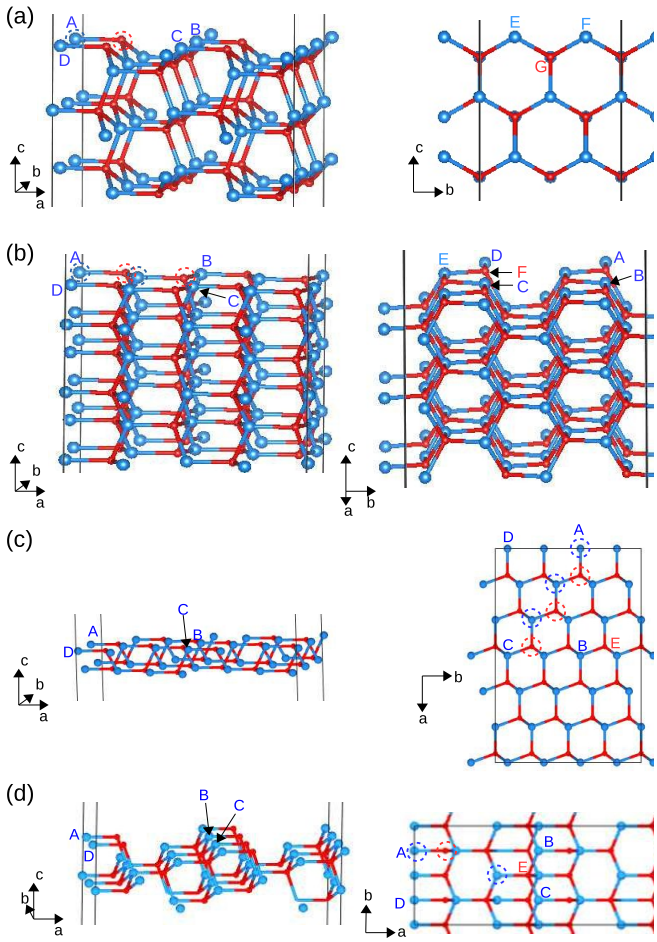

Fig. A1 (a)-(d): surfaces $(10\bar{1}0)$, $(11\bar{2}0)$, (110), and (211). In all cases, the polar axis is along vector a. The dashed circles highlight the surface atoms in a 1×1 cell. Red: O, blue: Zn.

For an ideal wurtzite ZnO structure, if the Zn-O bond length is d, then the thickness of a Zn-O double layer along the polar c axis is $4d/3$, and lattice constant c is $8d/3$. For zinc blende ZnO, the body diagonal of the cell is $3c/2$, or $4d$.

The top surface of slab $(10\bar{1}0)$ (Fig. A1(a)) is a 2×2 cell. Rectangle ABCD represents a 1×1 cell, which contains one O dangling bond and one Zn dangling bond. Distance AB is equal to lattice constant c. Distance AD is equal to EF, which can be calculated as follows. The projected length of segment EG on the paper plane is $l = \sqrt{d^2 - (d/3)^2} = \sqrt{8/9}d$, and therefore

EF=$2\times(l\times\sqrt{3}/2)=\sqrt{8/3}d$. The area ABCD is $(8/3)^{3/2}d^2$. Since area ABCD contains 2 dangling bonds, the dangling bond density is $3\sqrt{3}/(8\sqrt{2})d^{-2}$.

The top surface of slab $(11\bar{2}0)$ (Fig. A1(b)) is a 2×2 cell. The 1×1 cell ABCD contains two O and two Zn atoms and so four dangling bonds. Distance AB is equal to lattice constant c. Distance AD is equal to $3l$, where $l=\sqrt{8/9}d$ is the projection of bond EF on the plane normal to AB. The area ABCD is $(16\sqrt{2}/3)d^2$, resulting in a dangling bond density of $3/(4\sqrt{2})d^{-2}$.

The top surface of slab (110) (Fig. A1(c))is a 2×2 cell. The 1×1 cell ABCD contains three O and three Zn atoms and so six dangling bonds. Distance AB is equal to $4d$. Distance AD is equal to $3l$, where l is the projection of bond BE, which is on the paper plane, along AD. So AD is $3\times\sqrt{8/9}d=2\sqrt{2}d$. The area ABCD is $8\sqrt{2}d^2$ and so the dangling bond density is $3/(4\sqrt{2})d^{-2}$.

The top surface of slab (211) (Fig. A1(d)) is a 2×2 cell. The 1×1 cell ABCD contains one surface O atom which has two dangling bonds and two surface Zn atoms with one dangling bond each. AB is $4d$. AD is equal to $2l$, where l can be obtained from bond BE by first projecting BE onto the plane normal to AB and then projecting to the paper plane or ABCD. $l=\sqrt{8/9}d\times\sqrt{3}/2=\sqrt{2/3}d$. So the area ABCD is $8\sqrt{2/3}d^2$. Since area ABCD contains 4 dangling bonds, the density is $\sqrt{3/8}d^{-2}$.

References

1 J. Baxter, F. Wu and E. Aydil, *Appl. Phys. Lett.*, 2003, **83**, 3797–3799.

2 Z. Wang, X. Kong and J. Zuo, *Phys. Rev. Lett.*, 2003, **91**, 185502.

3 Y. Wang, B. Meyer, X. Yin, M. Kunat, D. Langenberg, F. Traeger, A. Birkner and C. Woll, *Phys. Rev. Lett.*, 2005, **95**, 266104.

4 B. Meyer and D. Marx, *Phys. Rev. B*, 2003, **67**, 035403.

5 B. Meyer, *Phys. Rev. B*, 2004, **69**, 045416.

6 C. R. A. Catlow, S. A. French, A. A. Sokol, A. A. Al-Sunaidi and S. M. Woodley, *J. Comput. Chem.*, 2008, **29**, 2234–2249.

7 M. Breedon, M. J. S. Spencer and I. Yarovsky, *J. Phys. Chem. C*, 2010, **114**, 16603–16610.

8 N. R. D'Amico, G. Cantele and D. Ninno, *J. Phys. Chem. C*, 2012, **116**, 21391–21400.

9 A. Ashrafi, A. Ueta, A. Avramescu, H. Kumano, I. Suemune, Y. Ok and T. Seong, *Appl. Phys. Lett.*, 2000, **76**, 550–552.

10 S. Kim, S. Jeong and C. Cho, *Appl. Phys. Lett.*, 2003, **82**, 562–564.

11 I. Suemune, A. Ashrafi, M. Ebihara, M. Kurimoto, H. Kumano, T. Seong, B. Kim and Y. Ok, *Phys. Status Solidi B-Basic Res.*, 2004, **241**, 640–647.

12 S. M. Zhou, H. C. Gong, B. Zhang, Z. L. Du, X. T. Zhang and S. X. Wu, *Nanotechnology*, 2008, **19**, 175303.

13 O. Chichvarina, T. S. Herng, K. C. Phuah, W. Xiao, N. Bao, Y. P. Feng and J. Ding, *J. Mater. Sci.*, 2015, **50**, 28–33.

14 Y. Ding, Z. L. Wang, T. Sun and J. Qiu, *Appl. Phys. Lett.*, 2007, **90**, 153510.

15 L. Lazzarini, G. Salviati, F. Fabbri, M. Zha, D. Calestani, A. Zappettini, T. Sekiguchi and B. Dierre, *ACS Nano*, 2009, **3**, 3158–3164.

16 J. Lv, F. Wang, Z. Zhou, C. Liu, W. Gong, Y. Feng, X. Chen, Y. Tang, G. He, S. Shi, X. Jiang, X. Song, Z. Sun and J. Cui, *Sci. Adv. Mater.*, 2013, **5**, 617–622.

17 A. Navrotsky, *Int. J. Quantum Chem.*, 2009, **109**, 2647–2657.

18 A. Navrotsky, *ChemPhysChem*, 2011, **12**, 2207.

19 C. Tang, M. J. S. Spencer and A. S. Barnard, *Phys. Chem. Chem. Phys.*, 2014, **16**, 22139.

20 R. S. Koster, C. M. Fang, M. Dijkstra, A. van Blaaderen and M. A. van Huis, *J. Phys. Chem. C*, 2015, **119**, 5648–5656.

21 P. J. Linstrom and W. G. Mallard, *NIST Chemistry WebBook (http://webbook.nist.gov), NIST Standard Reference Database No. 69*, National Institute of Standards and Technology, Gaithersburg MD, 2001.

22 H. Karzel, W. Potzel, M. Kofferlein, W. Schiessl, M. Steiner, U. Hiller, G. Kalvius, D. Mitchell, T. Das, P. Blaha, K. Schwarz and M. Pasternak, *Phys. Rev. B*, 1996, **53**, 11425–11438.

23 E. Kisi and M. Elcombe, *Acta Crystallogr. Sect. C-Cryst. Struct. Commun.*, 1989, **45**, 1867–1870.

24 A. Ashrafi, A. Ueta, A. Avramescu, H. Kumano, I. Suemune, Y. Ok and T. Seong, *Appl. Phys. Lett.*, 2000, **76**, 550–552.

25 G. Kresse and J. Furthmuller, *Phys. Rev. B*, 1996, **54**, 11169–11186.

26 G. Kresse and D. Joubert, *Phys. Rev. B*, 1999, **59**, 1758–1775.

27 P. Blöchl, *Phys. Rev. B*, 1994, **50**, 17953–17979.

28 J. Perdew, K. Burke and M. Ernzerhof, *Phys. Rev. Lett.*, 1996, **77**, 3865–3868.

29 M. J. S. Spencer, K. W. J. Wong and I. Yarovsky, *Mater. Chem. Phys.*, 2010, **119**, 505–514.

30 R. Kováčik, B. Meyer and D. Marx, *Angew. Chem.-Int. Edit.*, 2007, **46**, 4894–4897.

31 W. Göpel and U. Lampe, *Phys. Rev. B*, 1980, **22**, 6447–6462.

32 W. Göpel, L. Brillson and C. Brucker, *J. Vac. Sci. Tech.*, 1980, **17**, 894–898.

33 F. Fabbri, M. Villani, A. Catellani, A. Calzolari, G. Cicero, D. Calestani, G. Calestani, A. Zappettini, B. Dierre, T. Sekiguchi and G. Salviati, *Sci Rep*, 2014, **4**, year.

34 X. Shao, K.-i. Fukui, H. Kondoh, M. Shionoya and Y. Iwasawa, *J. Phys. Chem. C*, 2009, **113**, 14356–14362.

35 U. Diebold, L. Koplitz and O. Dulub, *Appl. Surf. Sci.*, 2004, **237**, 336–342.

36 T.-T. Chen, I.-C. Chang, M.-H. Yang, H.-T. Chiu and C.-Y. Lee,

Appl. Catal. B-Environ., 2013, **142**, 442–449.

37 S. Mukhopadhyay, P. P. Das, S. Maity, P. Ghosh and P. S. Devi, *Appl. Catal. B-Environ.*, 2015, **165**, 128–138.

38 K. M. Eblagon, P. Heydorn Concepcion, H. Silva and A. Mendes, *Appl. Catal. B-Environ.*, 2014, **154**, 316–328.

39 D. Gouvea, S. V. Ushakov and A. Navrotsky, *Langmuir*, 2014, **30**, 9091–9097.

40 K. Momma and F. Izumi, *J. Appl. Crystallogr.*, 2011, **44**, 1272–1276.